https://doi.org/10.5194/egusphere-2026-1633
Preprint. Discussion started: 18 May 2026

Horizontal sensible heat advection increases snow melt rates: Beyond point measurements

Eli Schwat[1], Michael Haugeneder[2], Dylan Reynolds[2], Daniel Hogan[1], Ethan Gutmann[3], and Jessica D. Lundquist[1]

[1]University of Washington, Civil and Environmental Engineering, Seattle, WA, USA
[2]WSL Institute for Snow and Avalanche Research SLF, Davos, Switzerland
[3]National Center for Atmospheric Research, Boulder, CO, USA

Correspondence: Eli Schwat (elilouis@uw.edu)

Abstract. In the atmospheric surface layer, it is generally assumed that vertical fluxes dominate near-surface heat transport and heat exchange between the atmosphere and the earth's surface. However, when the earth's surface is covered in patchy snow, near-surface horizontal advection of heat may be significant, and it's impact on snow melt rates is disputed. We estimated the contribution of horizontal sensible heat advection (Q_H) to snow melt using 8 days of measurements collected in May 2023 in the alpine East River basin in Colorado, Rocky Mountains, USA. We used an infrared video camera and polyester sheet to estimate Q_H, 3-meter resolution satellite imagery to track fractional snow covered area (fSCA), a scanning lidar to estimate snow melt rates, and micrometeorological and eddy covariance measurements to characterize the surface energy balance. Infrared camera measurements of Q_H over a single snow patch show that Q_H contributes to snow melt and is largest at the patch's upwind edge. Lidar-based snow melt measurements show that melt rates are highest at the upwind edge, further suggesting that Q_H causes snow melt. Over four days when fSCA was less than 62%, Q_H estimates ranged from 234–584 W m^{-2} and mid-day net radiation ranged from 331–508 W m^{-2}. When we considered only vertical heat fluxes, radiative fluxes, and snow melt in a snow patch surface energy balance equation, we found a mid-day residual between 267–668 W m^{-2}, and the residual increased as fSCA decreased. The approximate match between the energy balance residual and estimated Q_H suggests that advection is an important factor to consider when predicting snow melt. On days with low fSCA (< 62%), horizontal advection may contribute as much to snow melt as net radiation.

1 Introduction

In the atmospheric surface layer, it is generally assumed that vertical fluxes dominate near-surface heat transport and heat exchange between the atmosphere and the earth's surface. However, when the earth's surface is heterogenous, near-surface horizontal advection of heat may be significant. Horizontal heat advection has been identified as an important process near the coast (Mahrt et al., 2021), near forest boundaries (Kochendorfer and Paw U, 2011), within forest canopies (Thomas, 2011), and over patchy snow cover (Harder et al., 2017; Granger et al., 2006; Mott et al., 2018; Mahrt and Vickers, 2005). Horizontal heat advection over patchy snow is of particular interest, as the process may control snow melt speed and timing, and, as a result, the timing of spring streamflow. The magnitude of sensible heat advection over patchy snow has been estimated with numerical

https://doi.org/10.5194/egusphere-2026-1633
Preprint. Discussion started: 18 May 2026

atmospheric boundary layer simulations (Weisman, 1977; Liston, 1995; Claussen, 1991), measurements from horizontally distributed instrument towers (Harder et al., 2017; Granger et al., 2006; Essery et al., 2006; Mott et al., 2013, 2017), and, more recently, thermal infrared cameras (Haugeneder et al., 2023). From measurements, bulk theories have been developed to predict sensible heat advection rates over snow patches (Granger et al., 2002, 2006; Essery et al., 2006). Recently, snow ablation patterns resulting from horizontal advection have been measured with terrestrial laser scanning and structure-from motion methods (Van Der Valk et al., 2022; Mott et al., 2011). One-dimensional snowpack energy balance models are beginning to incorporate bulk theories for horizontal advection, with the goal of better representing snow melt in hydrologic systems (Harder et al., 2019).

The overall impact of horizontal heat advection on snow melt remains uncertain. Mott et al. (2015) found that sensible heat advection may be important during low fractional snow-covered area (fSCA), because upward heat fluxes over bare ground warm the atmosphere, which increases the heat content of air advected over patches of snow. In another study, Mott et al. (2013) found that stable internal boundary layers above snow patches may decouple from the overlying atmosphere, limiting the influence of advection on snow melt. This decoupling effect may be especially strong over topographic concavities, where snow patches often persist due to preferential deposition during blowing snow transport (Mott et al., 2016; Fujita et al., 2010). Further research is warranted to determine if horizontal heat advection significantly alters snow melt rates.

A major challenge to measuring the influence sensible heat advection on snow melt is that a large number of scalar and flux fields are relevant to the process. To directly estimate advection, one must measure the temperature field in the atmospheric surface layer that varies both horizontally and vertically across snow patch boundaries. Eddy covariance measurements of heat and momentum fluxes and wind speeds are needed to parameterize bulk models of advection. Radiation measurements and spatially distributed snow melt estimates are required to characterize the snow patch energy balance. To address uncertainty about snow melt processes, we deployed an exhaustive suite of instruments between November 2022 and June 2023 in the upper East River Valley of Colorado, Rocky Mountains, USA, as part of the Sublimation of Snow campaign (Lundquist et al., 2024).

During a period of patchy snow in the spring melt season, we utilized high resolution satellite imagery to characterize fSCA, an infrared video camera and polyester sheet to estimate horizontal sensible heat advection, a scanning lidar and fluidless snow pillows to estimate snow melt rates, and eddy covariance (EC) instruments and radiometers to characterize the snowpack surface energy balance. We used these measurements to answer the following research questions:

1. What is the magnitude of sensible heat advection?

2. What is the contribution of sensible heat advection to snow melt during patchy snow?

In the following, we first present our study site and our instrumentation. Then, we describe our methods, including how we estimated horizontal sensible heat advection over an isolated snow patch with an infrared video camera (following the methods of Haugeneder et al., 2023), how we estimated snow melt rates and the snow pack energy balance for individual patches of snow; and how we scaled our sensible heat advection estimates over a 300x300 m^2 area surrounding the measurement site. Finally, we present our results and discuss how our observations compare with those from previous studies.

https://doi.org/10.5194/egusphere-2026-1633
Preprint. Discussion started: 18 May 2026

2 Study site and instrumentation

We deployed flux towers, scanning lidars, and an infrared (IR) video camera to the Kettle Ponds site in the upper East River Valley, Rocky Mountains, USA between October 2022 and June 2023 (Figure 1). This deployment was part of the 9-month long Sublimation of Snow campaign (Lundquist et al., 2024). The Kettle Ponds site is on a relatively flat valley bottom, and micro-topography at the site is characterized by 2.5 meter tall ridges and swales (Figure 1a). Four instrument towers at the site had multiple eddy covariance (EC) systems and thermohygrometers mounted between 1 and 20 meters above ground level (AGL), a four-stream radiometer mounted at 9 meters AGL, four infrared radiometers for measuring surface temperature mounted at 3 meters AGL, and 6 scanning lidars mounted at 9.5 meters AGL, angled towards the ground. For this study, we used measurements from just one EC mounted on tower C, 3 meters AGL, and from two of the lidars, the scanning footprints of which are shown in Figure 1c. A full description of the instruments deployed and the EC data processing steps are provided by Lundquist et al. (2024) and Schwat et al. (2025), respectively.

During the snow melt season in seasonally snow covered landscapes, snow becomes patchy and the distribution of snow patches is spatially consistent across years due to consistent wind directions and increased deposition of snow in topographic depressions (Pflug and Lundquist, 2020; Schirmer et al., 2011). At Kettle Ponds, winds blow most frequently in the downvalley direction; and, during the spring melt of 2023, two distinct snow patches persisted in topographic depressions beneath towers UW and D (Figure 1c). These snow patches persist in similar locations year after year (Figure 1d–i). The footprints of our scanning lidars included the two distinct snow patches beneath towers D and UW (Figure 1c and g) and we were thereby able to measure the melt of the snow patches. Hourly camera images taken at the site in 2023 demonstrated that the first bare ground emerged on 7 May, and snow was completely gone from the site by 26 May. For this study, we focused on the patchy snow period between 10 and 17 May (Figure 2).

3 Methods

3.1 Theory for horizontal sensible heat advection over an isolated snow patch

In seasonally snow covered mid-latitude regions, such as the Rocky Mountains, during a spring day with patchy snow cover, bare ground temperatures can reach above 25 °C, while the surface of melting snow patches remains at 0 °C. Horizontal winds blow warmer air over snow patches, and, as the air passes over the snow surface, it is cooled. Close to the snow patch surface, where the air is cooled, an internal boundary layer (IBL) forms (Figure 3a). We define the IBL depth, $z_b(x)$, as the height where the temperature above the snow patch, $T(x,z)$, equals the temperature above the bareground area upwind of the snow patch, $T_u(z)$, i.e. $T(x,z_b) = T_u(z_b)$ (Figure 3a). For this study, we assumed that turbulence over the bare ground upwind of a snow patch is well-developed, and thus the temperature profile, $T_u(z)$, upward sensible heat flux, H_u, and wind speed profile, $U(z)$, over bare ground, are horizontally homogeneous.

The cooling of air that occurs within the IBL over a snow patch represents the extraction of sensible heat from the air by the snow patch. If the snow surface is below 0 °C, the snow will warm. If the snow surface is at 0 °C, the snow will melt.

https://doi.org/10.5194/egusphere-2026-1633
Preprint. Discussion started: 18 May 2026

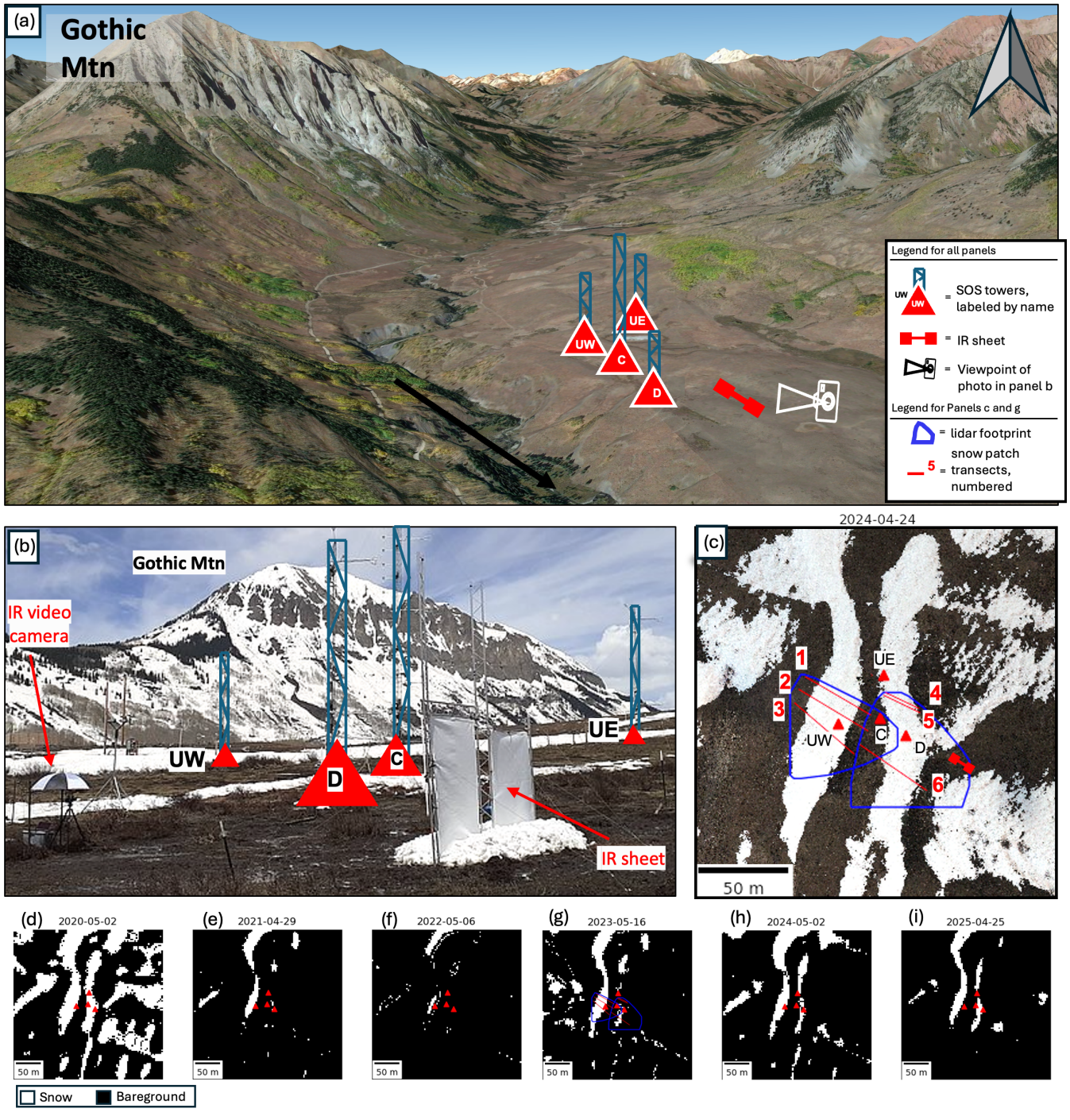

Figure 1. *Caption on next page.*

https://doi.org/10.5194/egusphere-2026-1633
Preprint. Discussion started: 18 May 2026

Figure 1. a) Oblique view of the upper East River Valley, looking upvalley (Source: Google Earth; Imagery ©2025 Airbus, Landsat, Copernicus). The approximate location of the Kettle Ponds site is shown with the relative location of the four towers. Tower locations are not to scale. b) Photograph of the infrared (IR) video camera with umbrella, IR observation sheet, and four towers. c) Orthoimage, collected by unmanned aerial vehicle on 24 April 2024. Red triangles show true tower lcoations. Blue lines show footprints of scanning lidars mounted on towers UE and C. Red lines show six transects for which we extracted lidar measurements. d–i) Fractional snow covered area (fSCA) maps derived from 3-meter resolution Planet imagery (PBC, 2020/2025) using PlanetSCA software (Yang et al., 2023; Chiu et al., 2025). fSCA maps on days from six separate years were selected to illustrate the consistent location of snow patches during the melt season. Includes copyrighted material of Planet Labs PBC. All rights reserved.

This means that horizontal advection of heat can increase snow warming and snow melt rates. Granger et al. (2002) proposed a boundary layer integration approach to estimating the total flux of energy into a snow patch, including advected sensible heat. This approach is derived by integrating the conservation of energy equation in two dimensions, over the Energy Control Volume illustrated in Figure 3a. We begin with a two-dimensional statement of conservation of energy,

$$U(z)\frac{\partial T}{\partial x} = \frac{1}{\rho c_p}\frac{\partial H}{\partial z}, \tag{1}$$

where ρ and c_p are the density and heat capacity of air, H is the downwards vertical sensible heat flux, U is the wind speed, which varies only in the vertical direction, and T is the temperature field, which varies horizontally and vertically (Essery et al., 2006). Integrating this equation across the Energy Control Volume (Figure 3a), horizontally from the upwind edge ($x = 0$) of a snow patch to the downwind edge ($x = X$), and vertically, from the patch surface ($z = 0$) to the IBL height ($z = z_b$), gives

$$\langle H_0 \rangle = H_u + Q_H \qquad | \qquad Q_H = \frac{\rho c_p}{X}\int_0^{z_b} U(z)\Big[T_u(z) - T(X,z)\Big]dz, \tag{2}$$

where H_u is the sensible heat flux above the bare ground upwind of the snow patch, Q_H is the advected sensible heat, and $\langle H_0 \rangle$ is the horizontally averaged sensible heat flux into the snow patch between $x = 0$ and $x = X$ (full derivation presented in Appendix A). With Equation 2, we can estimate $\langle H_0 \rangle$ using measurements or estimates of the sensib.e heat flux over the upwind bare ground (H_u), the wind profile, and the vertical temperature profiles at the up and downwind edges of the snow patch (e.g. Harder et al., 2017). Note that because we have defined z_b as the height, z, above snow where $T(x, z) = T_u(z)$, we can evaluate the integral in Equation 2 to any arbitrary height above z_b and find the same estimated advection.

Over the snow patch, the horizontal temperature gradient decreases with distance into the snow. This means that horizontal fluxes of sensible heat also decrease with distance into the snow, and this horizontal flux divergence is associated with the deposition of sensible heat into the snow patch below (horizontal red arrows in Figure 3a). Additionally, a vertical flux divergence exists above the snow patch, because the sensible heat flux is downward within the IBL and upward above the IBL (vertical red arrows in Figure 3a).

Note that an equation similar to Equation 2 could be defined for humidity (latent heat) fluxes using the conservation of water vapor equation. If the air is more humid over bare ground than over snow, transport of moister air over snow will result in

https://doi.org/10.5194/egusphere-2026-1633
Preprint. Discussion started: 18 May 2026

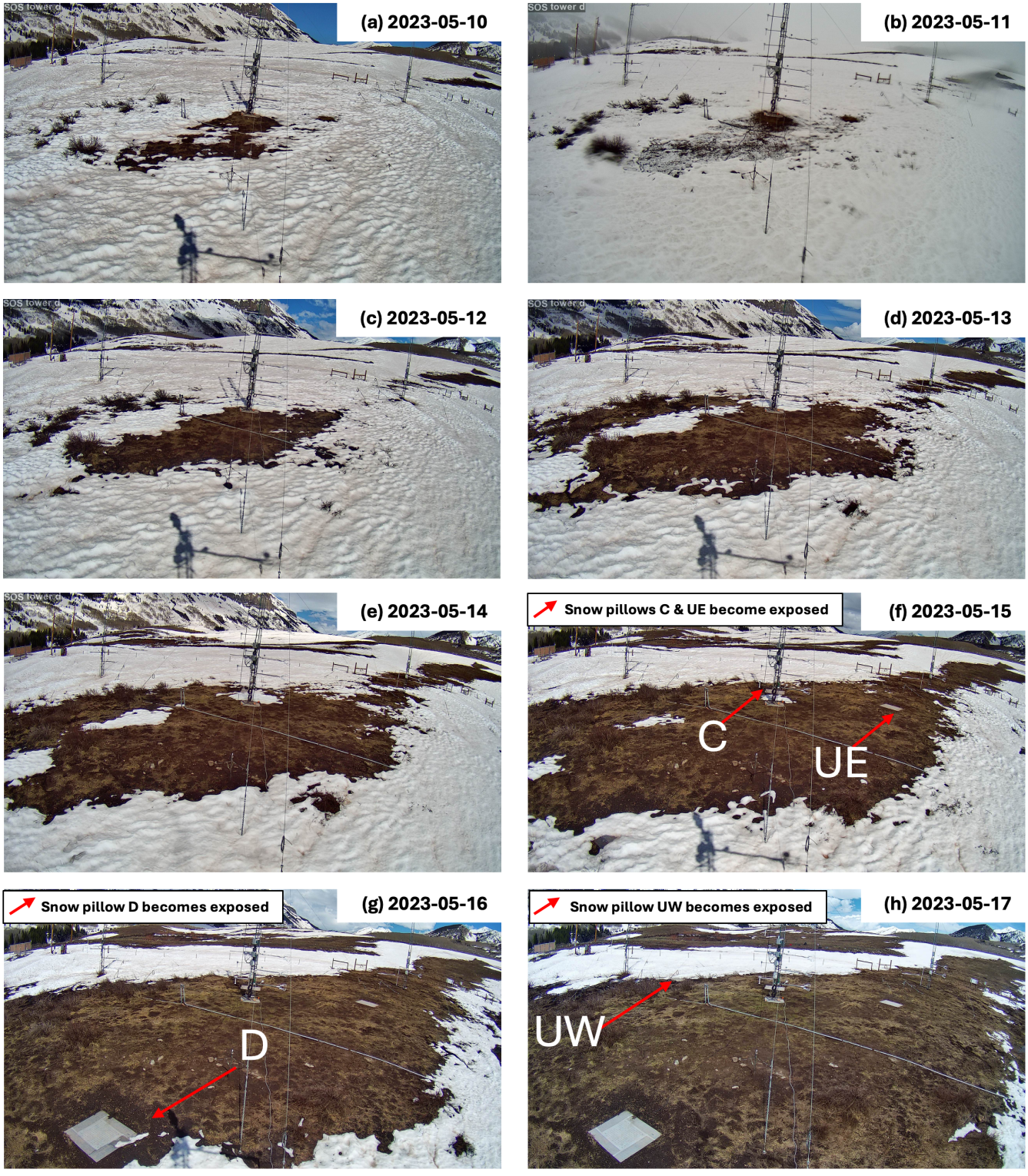

Figure 2. Images taken daily at 17:00 LT from a web camera mounted on tower D, pointed upvalley (Figure 1a). Arrows and labels in Panels f–h point to snow pillows situated near each tower.

https://doi.org/10.5194/egusphere-2026-1633
Preprint. Discussion started: 18 May 2026

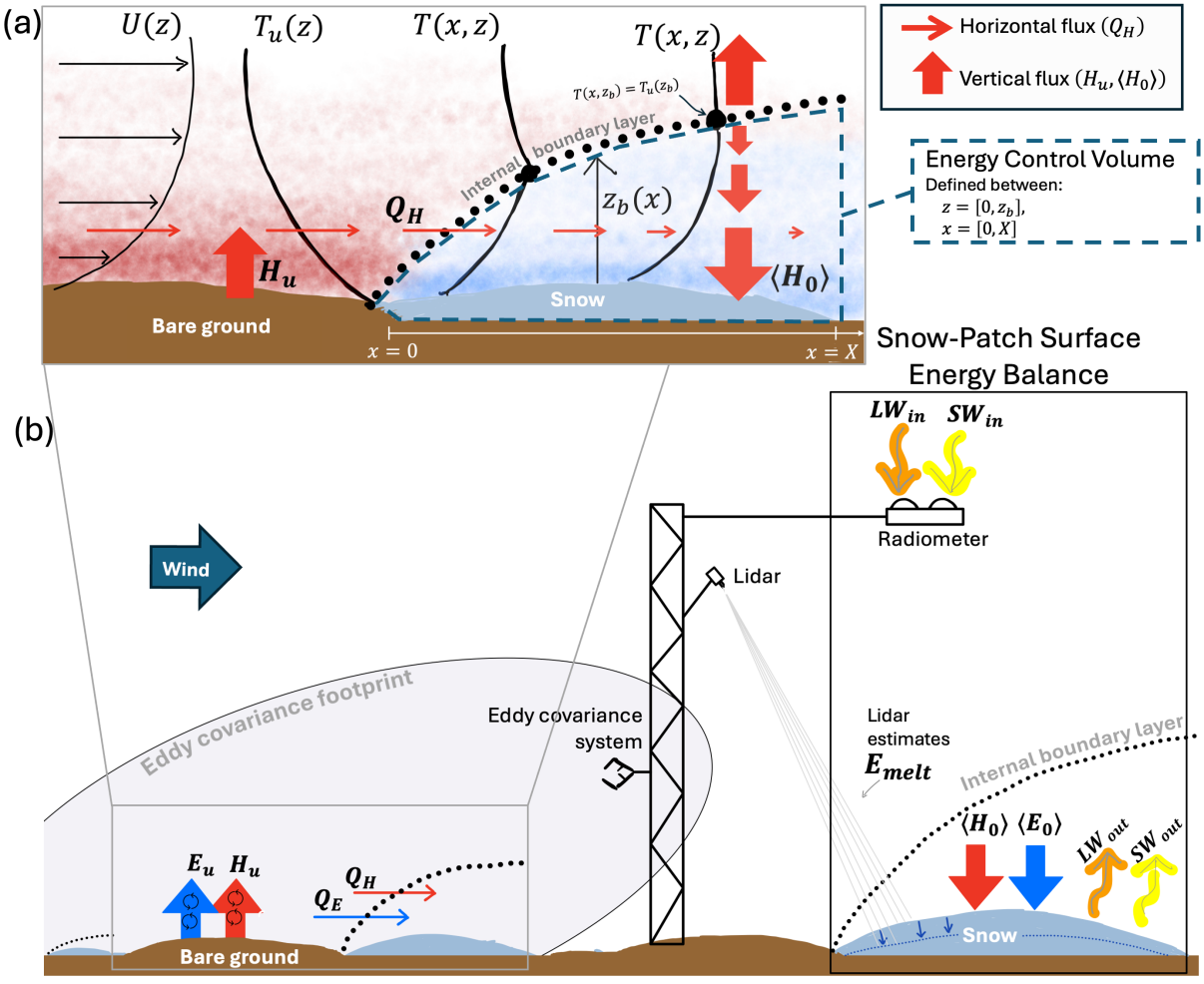

Figure 3. (a) Conceptual figure illustrating the development of an internal boundary layer (IBL) over a snow patch. $U(z)$ is the horizontal wind speed profile, which is assumed to be constant across bare ground and snow. $T_u(z)$ is the temperature profile over bare ground and $T(x,z)$ is the temperature profile over the snow, which varies with distance into the snow patch. $z_b(x)$ is the depth of the IBL formed over the snow patch, defined as the height where the temperature above snow equals the temperature above bare ground, i.e. $T(x,z_b) = T_u(z_b)$. H_u is the upward sensible heat flux over the bare ground, Q_H is the horizontally advected sensible heat, and $\langle H_0 \rangle$ is the horizontally-averaged sensible heat flux into the snow patch. Advected sensible heat (Q_H) decreases with distance into the snow patch and this horizontal flux divergence is associated with a deposition of heat into the snow patch. The conservation of heat equation (Equation 1) is integrated over the Energy Control Volume in the atmosphere over the snow patch, which is defined between $z = 0$ and $z = z_b$ and between $x = 0$ and $x = X$. (b) Conceptual diagram illustrating our approach to measuring the energy balance over a snow patch. The equivalent transport terms for latent heat fluxes are included ($E_u, Q_E, \langle E_0 \rangle$). The Snow-Patch Surface Energy Balance box includes all the terms in the energy balance equation (Equations 6 and 7). $\langle H_0 \rangle$ and $\langle E_0 \rangle$ are functions of terms outside the box, $\langle H_0 \rangle = H_u + Q_H$ and $\langle E_0 \rangle = E_u + Q_E$.

https://doi.org/10.5194/egusphere-2026-1633
Preprint. Discussion started: 18 May 2026

deposition of water onto the snow, which represents a heat flux into the snow. While we will not directly estimate latent heat advection in this study, we will consider its impacts on the snow energy balance. As above,

$$\langle E_0 \rangle = E_u + Q_E, \tag{3}$$

where E_0 is the horizontally averaged latent heat flux into a snow patch, E_u is the latent heat flux above exposed bare ground upwind of a snow patch, and Q_E is the advected latent heat.

3.2 Estimating horizontal sensible heat advection with an infrared video camera

On 17 May, a thin polyester sheet with an acrylate coating was rigged to a metal frame with elastic rope, oriented in the vertical plane and positioned over a snow patch (the "IR observation sheet" or "Polyster sheet", Figure 4a). The sheet material instantaneously adapts to the ambient air temperature, meaning the temperature of the sheet is the local air temperature. At the sheet, we pointed an Infratec VarioCAM HD thermal-infrared (IR) video camera, which recorded images of the sheet surface in the wave range 7.5–14 μm at 30 Hz. To minimize heating and cooling of the video camera, an umbrella was placed above it (Figure 1b, "IR video camera"). We converted the measured power to estimates of sheet-surface temperature using the Stefan-Boltzmann law and the emissivity of the sheet material, 0.94 (Haugeneder et al., 2023). Temperatures of the sheet, the snow below, and the surrounding landscape are shown in Figure 4b. Reflection and transmission by the surrounding environment and mean bias in the IR video camera's microbolometer are known to impact measured temperatures (Pestana et al., 2019). In this study, we only analyze relative differences in the measured temperatures (i.e. Equation 2), which are insensitive to these errors (Haugeneder et al., 2023). This method for measuring high resolution air temperatures was first presented by Grudzielanek and Cermak (2015) and further developed by Haugeneder et al. (2023).

The towers holding the sheet were stationary for the entire 2022–2023 winter. Upon arrival to the site on 17 May, no snow surrounded the towers. Snow was collected and piled around the towers to form a snow patch spanning the width of the observation sheets (Figure 4a). No snow was taken from near the instrumented towers (Towers UW, D, C, UE in Figure 1b), nor within the footprints of the scanning lidars (Figure 1c).

On 17 May 2023, thirty minutes of video were collected between 1200–1230, during which winds blew downvalley (from the left in Figure 4). We processed the video according to the following steps. First, we took the pixel-wise temporal mean across all 30 minutes (Figure 4b). Second, we trimmed the edges of the frames to exclude data outside the edges of the rigged sheet, and used the height and length of the metal supports to convert image pixels into real spatial dimensions, in meters. The pixel-resolution of each video frame is 5.4x5.4 mm. After trimming the frames, the left edge of the sheet begins at x = 0.08 m. We then removed pixels representing the snow surface by searching, in each column from the top down, for the first temperature measurement at or below 0 °C. That pixel, and pixels below it, are removed from the dataset. The result of these steps, a two-dimensional air temperature field, is shown in Figure 4c. We also calculated the temperature anomaly, defined as $T(x,z) - T_u(z)$, where $T_u(z) = T(x = 0.08, z)$, shown in Figure 4d.

We estimated Q_H and $\langle H_0 \rangle$ at various distances into the snow patch by extracting $T(x,z)$ at 25 cm intervals between $x = 0.25$ and 4.5m (Equation 2). We used measurements from the instrument towers to estimate the remaining inputs into

https://doi.org/10.5194/egusphere-2026-1633
Preprint. Discussion started: 18 May 2026

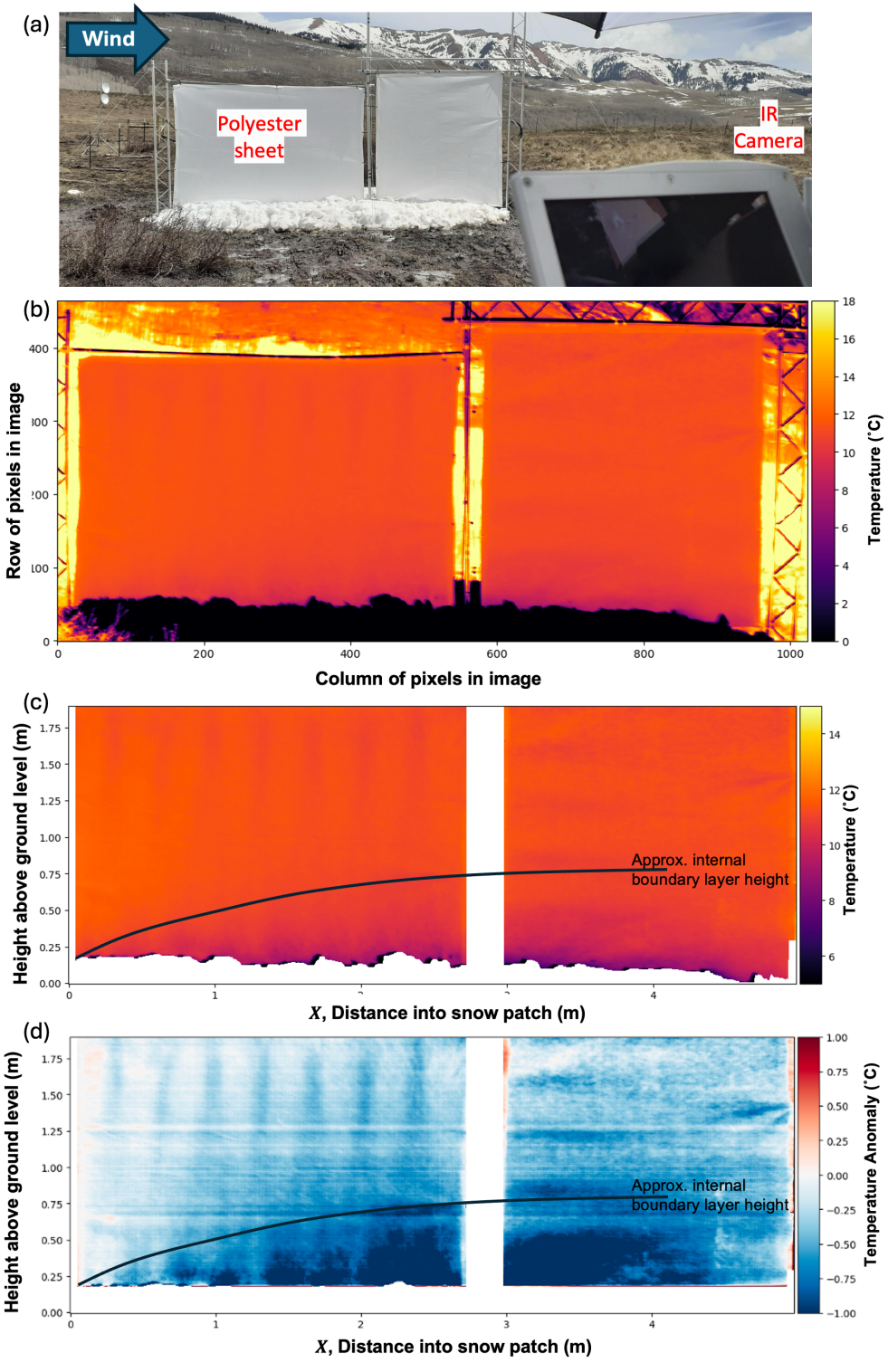

Figure 4. *Caption on next page.*

https://doi.org/10.5194/egusphere-2026-1633
Preprint. Discussion started: 18 May 2026

Figure 4. Illustration of the infrared video camera data collection method. a) Picture of the polyester observation sheet, from the vantage point of the infrared (IR) video camera. b) Mean measured temperature field, $T(x, z)$, observed by the IR video camera over 30 minutes, between 12:00–12:30 LT on 17 May 2023. Includes landscape behind the observation sheet. c) Same as panel b, but cropped to remove image pixels showing the landscape behind the observation sheet and the snow patch beneath. The black line approximates the internal boundary layer height, estimated and drawn by eye. d) Temperature anomaly field, defined as the difference between the measured temperature field and the vertical profile of temperature at the left edge of the IR observation sheet, $T(x, z) - T(x = 0.08, z)$. Temperature anomalies illustrate the height of the internal boundary layer, as well as systematic errors observed in the temperature field due to bends in the polyster sheet.

Equation 2. For H_u, we used the sensible heat flux measured by the EC at 3-meters AGL on tower C, between 12:00–12:30 LT. Theoretically, H_u should be constant upwind of the snow patch (Section 3.1). At 12:00-12:30 LT 17 May, H_u measurements made by four ECs at 3 meters AGL on four towers ranged from 130–170 W/m^{-2}. These estimates are within roughly 20% of each other, a common estimate of random error for EC flux measurements (Stiperski and Rotach, 2016). To estimate $U(z)$, we used the 3-meter EC measurement of U and shear velocity, $u_* = (\overline{u'w'}^2 + \overline{v'w'}^2)^{1/4}$, to calculate z_0 and fit the vertical velocity profile,

$$U(z) = \frac{u_*}{k} \ln\left(\frac{z + z_0}{z_0}\right). \tag{4}$$

This equation ignores the effects of atmospheric stability on the velocity profile, which is small in a shallow IBL (Essery et al., 2006). We calculated z_0 using measurements from an EC on tower C, which is approximately 50 meters upwind of the snow patch (Figure 1). The upwind fetch for tower C and the observation sheet are similar, so the calculated z_0 value is likely representative of the flow that interacts with the measured snow patch. Finally, we evaluated Equation 2 via numerical integration at each horizontal interval where we extracted $T(x, z)$ values. We integrated Equation 2 from 0 to $z_b = 0.75$ meters, which we visually determined is the upper limit of the IBL (Figure 4c and d). Although previous authors presented exponential forms for $z_b(x)$, we were not able to determine such an equation due to wavy errors created by creases and folds in the sheet (e.g. between x=[0,2] and z=[1.25, 2] in Figure 4c and d).

The numerical integrations result in estimates of $\langle H_0 \rangle$ and Q_H for distances into the snow patch, x. Because the sheet extended over the entirety of one snow patch, we can estimate the $\langle H_0 \rangle$ into the entire patch beneath the IR observation sheet. We will also estimate $\langle H_0 \rangle$ into snow patches of arbitrary width (Section 3.5). To do so, we used measurements of $Q_H(x)$ over the snow patch to fit the function

$$Q_H(x) = \alpha x^{\beta} \tag{5}$$

where α and β are fitted parameters and the exponential law describes the decay of $Q_H(x)$ with distance into the snow patch (Granger et al., 2002). α and β depend on wind velocity, snow and bare ground surface temperatures, and surface roughness (Harder et al., 2019). In our results, we present the fitted parameters and compare them with parameters presented in previous studies.

https://doi.org/10.5194/egusphere-2026-1633
Preprint. Discussion started: 18 May 2026

3.3 Measuring the snow pack energy balance

To estimate the relative contribution of sensible heat advection to the surface energy balance over a patch of snow (Research Question 2), we estimated the energy fluxes in a snow-patch surface energy balance,

$$E_{melt} = R_{net} + \langle H_0 \rangle + \langle E_0 \rangle = R_{net} + H_u + Q_H + E_u + Q_E, \tag{6}$$

where E_{melt} is the energy that goes towards melt of the snow patch and R_{net} is the horizontally averaged net radiative flux into the patch. R_{net} is the sum of the incoming longwave and shortwave radiation and outgoing longwave and shortwave radiation, $R_{net} = LW_{in} + SW_{in} - LW_{out} - SW_{out}$. Figure 3b diagrams the relevant energy fluxes and the instruments we used to measure them. Relative to other snow surface energy balance equations presented in the literature (e.g. Lundquist et al., 2024), ours is simple. We excluded the ground heat flux term, which characterizes heat from the earth warming the snow, the heat storage term, which represents changes in the temperature of the snowpack, and the heat flux from precipitation. Ground heat fluxes are generally small, on the order of 1 Wm^{-2}. During the melt season, snowpack temperatures do not fluctuate much. At Kettle Ponds and at another nearby site, the snowpack was isothermal and reached 0 °C by mid April 2023 (Lundquist et al., 2024; Cox et al., 2025). Similar simplifications to the energy balance were also made by Van Der Valk et al. (2022) in their patchy snow melt study.

We only measured Q_H on one day, 17 May, with the IR observation sheet, and we did not measure Q_E. We measured the remaining terms in the energy balance continuously throughout our study period. When we present energy balance results, we use the following form of the energy balance,

$$E_{melt} = R_{net} + H_u + E_u + Res, \tag{7}$$

where Res is calculated from the other measured terms in Equation 7. Non-zero Res could be explained by non-zero Q_H or Q_E, by other energy fluxes we do not account for, such as heat storage in the air or snow, or by error in our measurements. We estimated each term in Equation 7 at hourly resolution for the duration of our study period. Below, we describe how we estimated each term.

3.3.1 Estimating E_{melt} with snow pillows and scanning lidar

We estimated E_{melt} using four, fluidless snow pillows and two scanning lidars deployed at Kettle Ponds. Snow pillows are scales that are buried into the dirt such that a 0.9x0.9 m^2 (3x3 ft^2) scale platform is flush with the ground surface. One snow pillow was deployed near the base of each tower at the site (e.g. Figure 2f–h). The pillows recorded the snow water equivalent (in units of meters) on the scale throughout the winter season at a 5 minute resolution, which we upsampled to hourly means. The snow pillow measurements contain a diurnal systematic error associated with temperature fluctuations. We applied a cumulative minimum to the hourly time series to remove erroneous increases in snow mass. We then calculated the rate of snow mass change, $\frac{\mathrm{d}SWE}{\mathrm{d}t}$ (m/hr), by differentiating the time series using the second order central difference. Finally, we calculated the hourly melt energy (in W/m^{-2}) assuming the specific heat of fusion is $L_f = 334$ kJ/kg and the density of water

https://doi.org/10.5194/egusphere-2026-1633
Preprint. Discussion started: 18 May 2026

is $\rho_w = 1000$ kg/m^3,

$$E_{melt} = L_v \rho_w \frac{\mathrm{d}SWE}{\mathrm{d}t}. \tag{8}$$

Equation 7 describes the surface energy balance averaged over a snow patch. However, snow pillow estimates of E_{melt} are representative of a very limited area. Estimates of E_{melt} over the full extent of a snow patch are more appropriate for our snow-patch surface energy balance approach (Figure 3b). During our study period, two scanning lidars continually observed the melt of the two distinct snow patches that formed underneath towers UW and D (Figures 1c). We estimated E_{melt} with the scanning lidar measurements and evaluated the lidar-based estimates with the snow pillow-based estimates.

The lidars scanned and generated a point cloud every 5 minutes, but we only used point clouds collected at the beginning of each hour. From the lidar point clouds, we generated a time series of gridded digital surface models (DSMs) with 5 cm horizontal resolution. For each grid cell, we assigned the minimum elevation of all points falling within that cell. Due to reflection of light across variable snow surfaces and the emergence of vegetation during our study period, hourly DSMS contained significant noise. To reduce noise, we manually selected six horizontal transects with limited noise and calculated snow depth changes only along the transects (Figure 1c). For each pixel in the hourly transects, we applied a cumulative minimum function, same as for the snow pillows. We then calculated the pixel-wise rate of snow depth change (m/hr) by differentiating each pixel's time series of surface elevation using the second order central difference. Finally, we calculated the hourly melt energy for each transect by averaging snow depth change across all pixels. The six transect-averaged snow depth change rates are then converted to melt energy using the specific heat of fusion (L_f) and by assuming a constant snow density of $\rho_{snow} = 550$ kg/m^3, which we found is a realistic density for melting snow at Kettle Ponds (Appendix B),

$$E_{melt} = L_f \rho_{snow} \frac{\mathrm{d}h_{snow}}{\mathrm{d}t}. \tag{9}$$

3.3.2 Estimating R_{net}

To estimate R_{net}, we used measurements of LW_{in} and SW_{in} collected by a Hukseflux NR01 4-stream radiometer, mounted on tower UW. We did not use the radiometer's measurements of outgoing radiation, as we are considering an energy balance at the surface of a snow patch, and the radiometers downward facing sensors have a field of view that included both bare ground and snow during our study period (Figure 3b). We calculated LW_{out} for a snow patch using the Stefan-Boltzmann equation,

$$LW_{out} = \sigma \epsilon T_s^4 \tag{10}$$

where σ is the Stefan-Boltzmann constant, 5.67e^{-8} W m^{-2} K^{-4}, ϵ is the emmisivity of snow, which we set to 0.98 (Raleigh et al., 2013), and T_s is the snow surface temperature. We used the infrared radiometer deployed on tower UW to measure T_s. Although we deployed infrared radiometers on all four towers, only the UW instrument had snow within its field of view for the entirety of the study period. We calculated SW_{out} for a snow patch by assuming a snow albedo of 0.6, which was the albedo measured over the snow at Kettle Ponds in early May, before snow became patchy (Lundquist et al., 2024).

https://doi.org/10.5194/egusphere-2026-1633
Preprint. Discussion started: 18 May 2026

3.3.3 Estimating H_u and E_u

To estimate H_u and E_u, we used 30-minute EC measurements from the Kettle Ponds site, upsampled to hourly averages. Ogive analysis (not shown) indicated that 30-minutes is an appropriate Reynolds averaging timescale for both fluxes (Foken et al., 2006; Schwat et al., 2025). Note that for our snow-patch surface energy balance approach, H_u and E_u should be the heat fluxes over bare ground upwind of a snow patch (Figure 3a). However, EC instruments measure aggregated fluxes over a large footprint (Figure 3b), and upwind of the instrument towers, during our study period, there is both snow and bare ground (Figure 1g). This means that the measured E_u and H_u may be lower than true fluxes over just bare ground. We discuss this issue further after presenting our results.

3.4 Measuring fractional snow covered area with high resolution satellite imagery

To characterize fractional snow covered area (fSCA, e.g. Figures 1d–i) over the Kettle Ponds site and the surrounding area, we used Planet imagery, which provides near-daily coverage at 3-meter resolution (PBC, 2020/2025). To identify fSCA, we used a pre-trained Random Forest model ("PlanetSCA") that classifies each pixel in an RGB image as snow or not snow (Yang et al., 2023; Chiu et al., 2025). We used 11 Planet images in this study. This includes one melt-season image for each from 2020–2025, which show consistent snow patch patterns at Kettle Ponds (Figure 1d – i), and all available images with minimal cloud cover from the 10–17 May 2023 study period and surrounding dates (Figure 10di–dvi). We then cropped each image to a $\pm$150 meter square cenetered on tower C at Kettle Ponds and used PlanetSCA to create fSCA maps. These maps cover a 300x300 m^2 area.

3.5 Estimating horizontal sensible heat advection across the landscape

Our formulation of the snow patch surface energy balance (Equation 7) includes a residual term, Res. According to Equations 6 and 7 and ignoring the neglected energy terms, this residual represents the combined contribution of horizontal sensible and latent heat advection. To address our second research question, we compare Res to our independent estimates of horizontal sensible heat advection (Q_H), which allows us evaluate how much horizontal advection contributes to snowmelt. If both the residual and our advection estimates are large, this would support the conclusion that advection plays a significant role in melting the snow.

We measured Q_H over a single snow patch for 30-minutes on 17 May using an IR video camera (Section 3.2), but we wanted estimates across the study period to compare energy balance terms. To do this, we fitted Equation 5 using IR camera measurements from 17 May, and used the fitted equation to Q_H as a function of snow patch width. We first estimated the distribution of snow patch widths surrounding Kettle Ponds from fSCA maps on 4 days. We drew 105 lines across the domain, oriented along the dominant wind direction (315°) and spaced 5 m apart (Figure 5a). Along each line, we identified all continuous snow-covered segments in each of the 2023 fSCA images (Figure 5b), which creates a sample distribution of snow patch widths for each day with an fSCA image. We then plug in the patch width distributions for x in Equation 5 to estimate a corresponding sample distribution of Q_H. The Q_H distributions represent the range of horizontal sensible heat advection

https://doi.org/10.5194/egusphere-2026-1633
Preprint. Discussion started: 18 May 2026

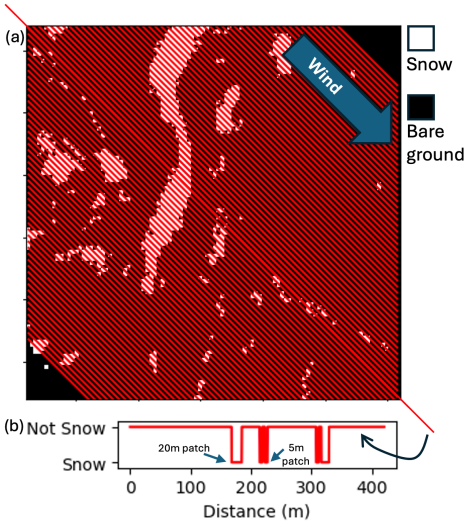

Figure 5. a) fSCA map from 2023-05-16 (recreated from Figure 1g), overlayed with lines aligned with the wind direction. b) Example of values extracted from the fSCA map along one line. Continuous segments of snow define the width of snow patches encountered in the along-wind direction.

fluxes occurring across the 300x300 m^2 study domain. We only report results for days with fSCA is smaller than 62%, because at higher fSCA the landscape shifts to having isolated bareground patches within snow, a situation for which Equation 5 is not suited (see Section 3.1).

4 Results and Discussion

4.1 Estimating advective sensible heat fluxes with an infrared camera

To answer Research Question 1, we measured sensible heat flux into a snow patch, $\langle H_0 \rangle$, using the infrared camera data and Equation 2 . First, we calculated the aerodynamic roughness length and found $z_0 = 0.0079$ m, which is consistent with the observed surface composed of a mix of mud flats ($z_0 = 0.005$ m) and flat terrain with isolated obstacles ($z_0 = 0.03$ m) (Wieringa, 1980). Our $\langle H_0 \rangle$ estimates from the infrared video camera are shown as dots in Figure 6. Within the first 75 cm of the patch, $\langle H_0 \rangle$ increases, reaching above 800 W m^{-2} at $x = 0.75$ m, and then decreasing to around 200 W m^{-2} by $x = 4.5$ m. The observed decay in $\langle H_0 \rangle$ with distance into the patch is predicted by theory. With distance into the snow patch, the IBL depth grows, the horizontal temperature gradient decreases, and Q_H decays (visible in Figure 4d, illustrated in Figure 3a). Granger et al. (2002) predicted that the decay would follow a power law, Equation 5, with b = -0.47 for strong turbulence. When we excluded the two measured data points between $x = 0$ and $x = 0.75$ m, we found b=-0.54 (0.5368 ± 0.0015 using a 10% confidence interval), and the curve fits most of the data points closely (Figure 6, orange line). Van Der Valk et al. (2022) used direct numerical simulation to estimate sensible heat advection over snow patches and estimated b=-0.35. The initial increase

https://doi.org/10.5194/egusphere-2026-1633
Preprint. Discussion started: 18 May 2026

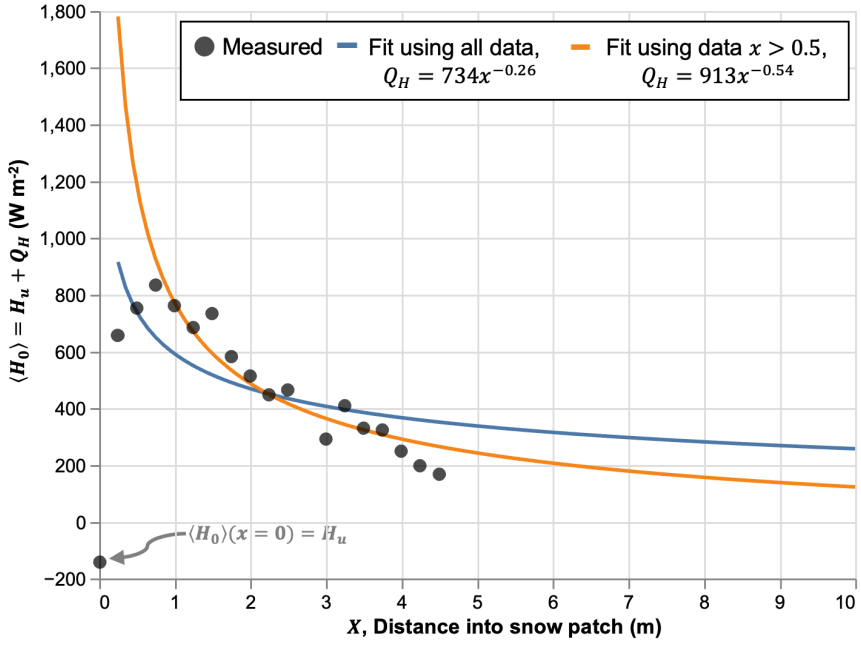

Figure 6. Average downward heat flux by snow patch width, measured (grey points) and modeled (blue and orange liens). Measured data are calculated using Equation 2 and the mean temperature field collected over 30-minutes by the infrared video camera (Figure 4c). Modeled lines represent Equation 5 fitted to the measured data using the least squares method. The blue line was fit including all measured points, the orange line was fit to all measured points for $x > 0.5$m.

in $\langle H_0 \rangle$ could be due to the fact that our snow patch was piled approximately 20 centimeters above the ground (Figure 4a). The height of the snow pile forces flow approaching along the ground to rise, which could lead to flow separation and decreased turbulent exchange at the windward edge. Another possibility is that the rigid metal frame holding the screen disrupted the flow. Overall, our data conforms to established theory quite well, apart from the initial increase in $\langle H_0 \rangle$ in the first 75 centimeters of the snow patch. When we fit the power function to all the measured data, we found b=-0.23 (Figure 6, blue line), which is outside the range of possible parameter values predicted by Granger et al. (2002). Our measurements beyond $x = 75$ cm also appear more linear than exponential, suggesting that existing exponential models are incorrect. However, previous studies measured horizontal sensible heat advection and snow melt across larger snow patches (Granger et al., 2006; Mott et al., 2011), and the linear appearance of our measurements may simply be because our snow patch is relatively short. Future IR camera deployments could attempt to measure high resolution temperature fields over wider snow patches to confirm or deny exponentially decaying Q_H and $\langle H_0 \rangle$. In any case, the decent match between $\langle H_0 \rangle$ measurements and predictions led us to use the fitted function (Figure 6, orange line) to estimate sensible heat advection over other patches near the site.

https://doi.org/10.5194/egusphere-2026-1633
Preprint. Discussion started: 18 May 2026

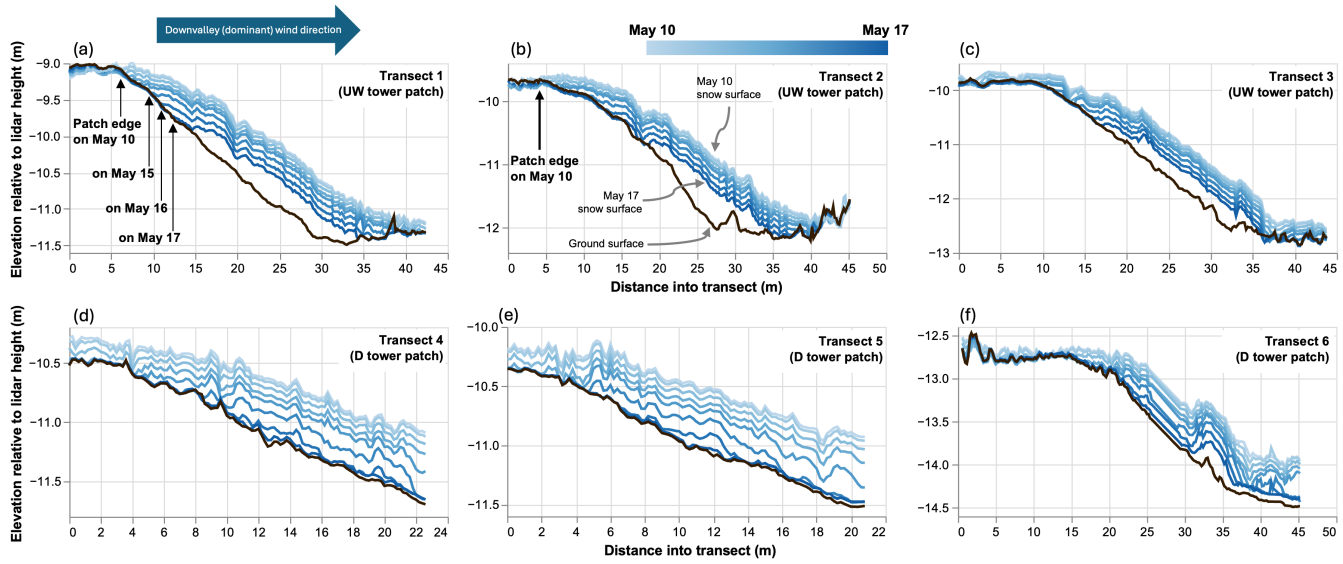

Figure 7. Surface elevations extracted over the six transects (Figure 1c) from lidar scans. One surface elevation transect is shown for each day between 10–17 May, from the scan collected at 00:00 LT. Blue lines show the changing snow surface. The black line shows the underlying topography. In panels a and b, black arrows point to the upvalley edge of the snow patch. Vertically exaggerated by 10x.

4.2 Monitoring snow patch evolution with scanning lidar

We calculated hourly snowmelt rates for 10–17 May from six 1-dimensional transects of surface elevation over melting snow patches. Before examining the snow melt rates, we examined the evolution of the transect snow surface elevations, shown in Figure 7. The transect numbers in Figure 7 correspond to the numbered transects in Figure 1c. Figures 7a, b, and c show the melt out of the snow patch beneath tower UW and illustrate that snow patches persisted in concave topography. By 17 May, the uphill side of all the patches receded below the top of the local topographic highs (e.g. Figure 7a, see "Patch edge"). Figures 7d, e, and f show the melt out of the snow patch beneath tower D. Transects over this patch clearly show that melt rates accelerated between 10–17 May. They also show that the tower D snow patch had mostly disappeared by 16 May. Therefore, beginning on 16 May, snowmelt rate estimates include only measurements from transects 1–3 (Section 3.3.1). Across all six transects, the average rate of snow surface elevation change was -2.8 mm/hr, which corresponds to an average melt rate of 1.5 mm SWE/hr (accounting for our snow density estimate of 550 kg/m^3). Note that surface lowering and melt rates were only calculated for positions on the transects where snow existed throughout the study period.

Our measurements of transects 1 and 2 capture the uphill, upvalley edge of the snow patch from the beginning of the measurement period on 10 May (Figures 7a and b, see "Patch edge"). Using these two transects, we examined how melt rates varied with distance from the upwind patch edge. We calculated the mean of melt rates binned by distance from the patch edge, and adjusted the location of the patch edge at the beginning of each day to follow its movement as it receded downslope (e.g. Figure 7a). We then normalized the bin-averaged melt rates by the time-and-space-averaged melt rate (Figure 8). To maintain

https://doi.org/10.5194/egusphere-2026-1633
Preprint. Discussion started: 18 May 2026

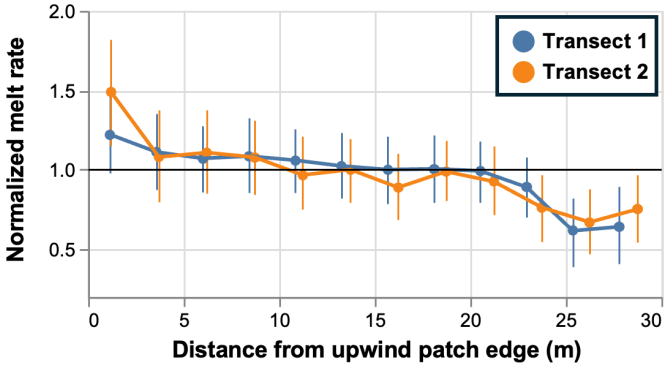

Figure 8. Normalized, temporally-averaged snow melt rates for snow patch transects 1 and 2 (shown in Figure 7a and b) Rates are normalized by the temporally and spatially averaged rate, and then temporally-averaged. Dots show mean melt rate binned by distance from the upwind patch edge, data is only included when winds are blowing downvalley (e.g. from the left in Figure 7). Bars show the 95% confidence interval around the mean; we assumed errors are normally distributed.

a consistent upwind patch edge, we only included measurements when winds blew downvalley, which comprised 73% of our study period. We assumed that errors from lidar measurements are normally distributed, and show both the mean melt rate for bins of distance-from-patch-edge and the 95% confidence interval around that mean. Melt rates generally decreased with distance from the upwind patch edge. For both transects, melt rates within 5–10 meters of the upwind patch edge were between 1.2–1.5 times larger than average melt rates, and melt rates greater than 20 meters from the patch edge were 0.6–1.0 times the average rate (Figure 8). We found that melt rates increased at the upwind edge of a snow patch in a topographic depression, suggesting that horizontal advection contributed to snow melt. Because horizontal heat advection decays with distance into a snow patch (Figure 6), melt rates should decay as well.

These results are similar to previous findings, with some slight differences. Van Der Valk et al. (2022) measured melt rates at the front and back edges of a snow patch and found that melt rates at the front edge were 1.8 times higher than average. Mott et al. (2011) measured melt rates with lidar and found that melt rates decreased exponentially with distance into the snow patch, with melt rates at the front edge 1.1–1.6 times higher than average, and melt rates beyond 5 meters into the patch lower than average. Our measurements diverge from the findings of Mott et al. (2011) in that below-average melt rates were only found in our measurements nearest to the downwind snow patch edge, beyond 20 meters into the patch. (Figure 8)

Snow patches are known to form in topographic depressions, due to preferential deposition during blowing snow transport. Previous authors have hypothesized that snow patches in topographic depressions may experience reduced heat fluxes due to lower wind speeds in the depressions and atmospheric decoupling (Mott et al., 2015), which further preserve the snow patch in a self-regulating manner (Fujita et al., 2010). In one study in the Swiss Alps, Mott et al. (2013) found that snow ablation rates measured over a snow patch within a depression were smaller than ablation rates of patches on slopes. We found that melt rates measured over a snow patch in a depression (the UW tower patch, Figures 7a–c) were actually larger (1.71 mm SWE/hr) than melt rates measured over a snow patch not in a depression (1.36 mm SWE/hr, the D tower patch, Figures 7d–f). We also

https://doi.org/10.5194/egusphere-2026-1633
Preprint. Discussion started: 18 May 2026

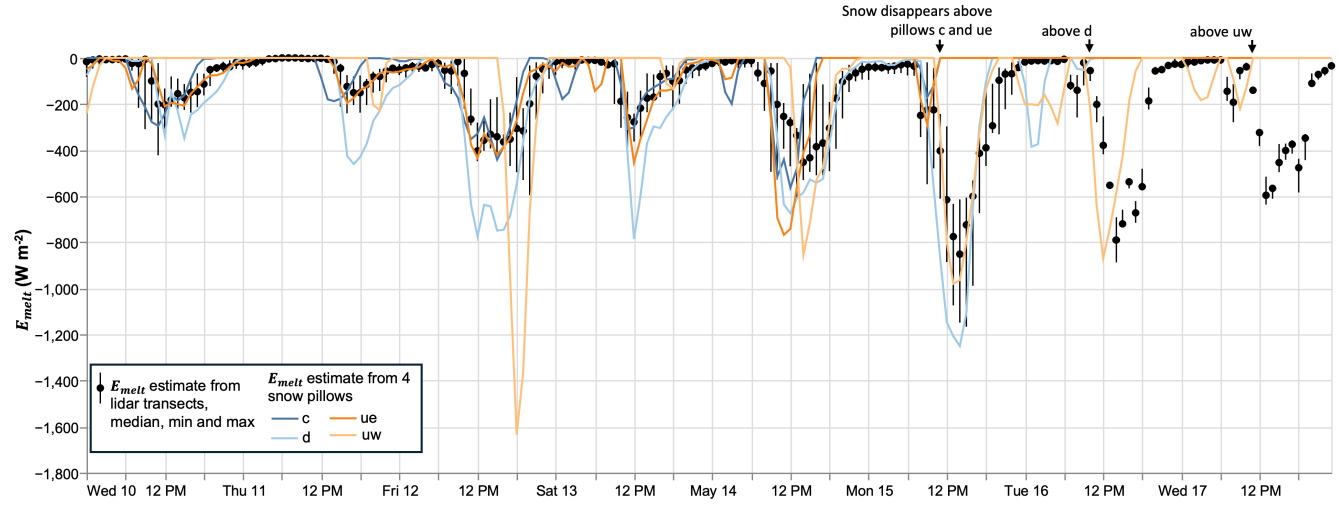

Figure 9. Melt energy estimated from snow pillows and lidar. Snow pillow and lidar change rates are calculated using second order differencing. Lidar surface elevation change rates are converted to mass change rates assuming a snow density of 550 kg/m^3, estimated from snow pillow measurements of SWE and lidar measurements of snow depth. Black dots and bars show the median and IQR of E_{melt} estimates from six snow patches. The colored lines show the E_{melt} estimates from the four snow pillows. Snow melted out above the snow pillows throughout the study period; these times are indicated by arrows and the snow pillows become visible in Figure 2.

observed that melt rates increased over our study period (visible in Figures 7a, d and e), even as snow patches receded below upwind topographic highs and were therefore theoretically more protected from winds. We concluded that decoupling was not important at our site.

4.3 Estimating snow melt energy with scanning lidar and snow pillows

From the lidar measurements, we calculated the vertical snow surface decay rates for six transects and converted to snow melt rates ("lidar-based melt rates") using a snow density of 550 kg m^{-3} (Section 3.3.1). We compared lidar-based melt rates with the rates measured by four snow pillows. The snow pillow melt rates and the mean, minimum and maximum of the lidar measurements are shown in Figure 9. The two methods for estimating snow melt generally agreed. Snow melt rates generally increased over the study period, and 15–17 May had the highest daily melt rates. On 15 May, snow melted out above the snow pillows at towers C and UE (Figures 9 and 2f). By 17 May, snow had melted out above the tower D and UW snow pillows (Figures fig:emelt-lidars-and-snow-pillows and 2g and 2h). Between 10–14 May, the UW snow pillow showed little melt, with an unusuaully large melt rate on 12 May. This could due to pooling of water in the snowpack which compensated for any mass lost to melt (Lundquist et al., 2024) or due to snow-bridging, when a hard layer in the snowpack forms and reduces pressure on the pillow scale (Sorteberg et al., 2001). Excluding the UW snow pillow and dates after 13 May when snow above the pillows began disappearing, mean lidar and mean snow-pillow melt rates were correlated with an r^2 of 0.53. Snow pillow melt rates were, on average, 24% larger than pillow rates. Excluding the UW and D snow pillows, mean lidar and mean snow-pillow melt

https://doi.org/10.5194/egusphere-2026-1633
Preprint. Discussion started: 18 May 2026

rates were correlated with an r^2 of 0.69 and melt rates matched within .01%. For our purpose of characterizing the snowpack energy balance over the entire study period, the lidar melt rate measurements were more useful because they produced reliable snow melt rates after snow disappeared above the snow pillows.

4.4 Snow melt and the surface energy balance including horizontal advection

To estimate the contribution of horizontal sensible heat advection to the energy balance over patchy snow (Research Question 2), we estimated all fluxes in the energy balance (Equation 7) and compared them during the onset of snow patchiness at the site. Snow became patchy at the Kettle Ponds site by, at the latest, 13 May, when surface temperatures near two of four towers rose above 0° (Figure 10a). Images of the site show that bareground patchy by 12 May (Figure 2b–c). Snow cover dominated the site through 13 May, when fSCA was still 62% (Figure 10diii). By 15 May, fSCA dropped to 18% (Figure 10div). No satellite imagery nor fSCA maps were available for 14 May. We consider the onset of the patchy snow period to be 15 May, when fSCA dropped below 50% and the land surface shifted from bare ground patches within snow (Figure 10iii) to snow patches within bare ground (Figure 10iv).

Before 13 May, H_u was positive (Figure 10c), indicating downward transport of sensible heat, which is common over snow because the atmosphere is generally warmer than the snow surface in the middle of the day. Starting on 14 May, H_u was consistently negative, indicating upward heat fluxes and suggesting that bare ground dominated the EC footprint. E_u was negative (upward) or near-zero throughout the study period, representing evaporation or sublimation. Interestingly, both H_u and E_u remained near zero on 13 May. This implies that, within the EC footprint, all heating of the atmosphere by bare ground was balanced by cooling of the atmosphere by snow, and all evaporation over bare ground was balanced by condensation onto snow. This also implies that horizontal transport of sensible and latent heat had begun.

Net radiation followed a typical diurnal solar cycle (Figure 10c). Intermittent cloud cover produced midday dips in net radiation (e.g., 12 May at 12:00). At night, slightly negative net radiation indicated longwave cooling of the surface, consistent with the gradual decrease in surface temperatures (e.g., 1800 12 May – 0600 13 May and 1800 15 May – 0600 16 May, Figures 10a and c). Estimates of snow melt energy (E_{melt}) followed the diurnal cycle of net radiation, and were generally larger in magnitude than R_{net} (Figure 10c).

We calculated Res from the other energy flux terms (Equation 7). In Figure 10c, the spread in Res reflects the spread in E_{melt}. For most of the study period, Res was non-zero, indicating that the energy flux terms we measured did not balance all the observed snowmelt. During many days, the morning transition (0900–1100) was characterized by a negative Res, meaning that more energy was provided by radiation and turbulent heat fluxes than was used by melting snow. This extra energy may have gone towards warming up the snowpack. While the snow surface warmed to zero by 0700–0800 on most days and the negative residual occurred between 0900–1100, snow beneath the surface may have remained below 0°C later into the day (e.g., 0600-1200 16 May, Figures 10a and c). Starting on 12 May, Res became positive between 0600–1200 each day, remained positive through the daytime, and returned toward zero between 1800–2400 as E_{melt} decreased to zero. Before 14 May, when fSCA $> 50\%$, the mean daily energy balance residual was ≤ 54 W m^{-2} (Figure 10b) After 14 May, when fSCA $< 50\%$, the mean daily residual ranged from 90–173 W m^{-2}.

https://doi.org/10.5194/egusphere-2026-1633
Preprint. Discussion started: 18 May 2026

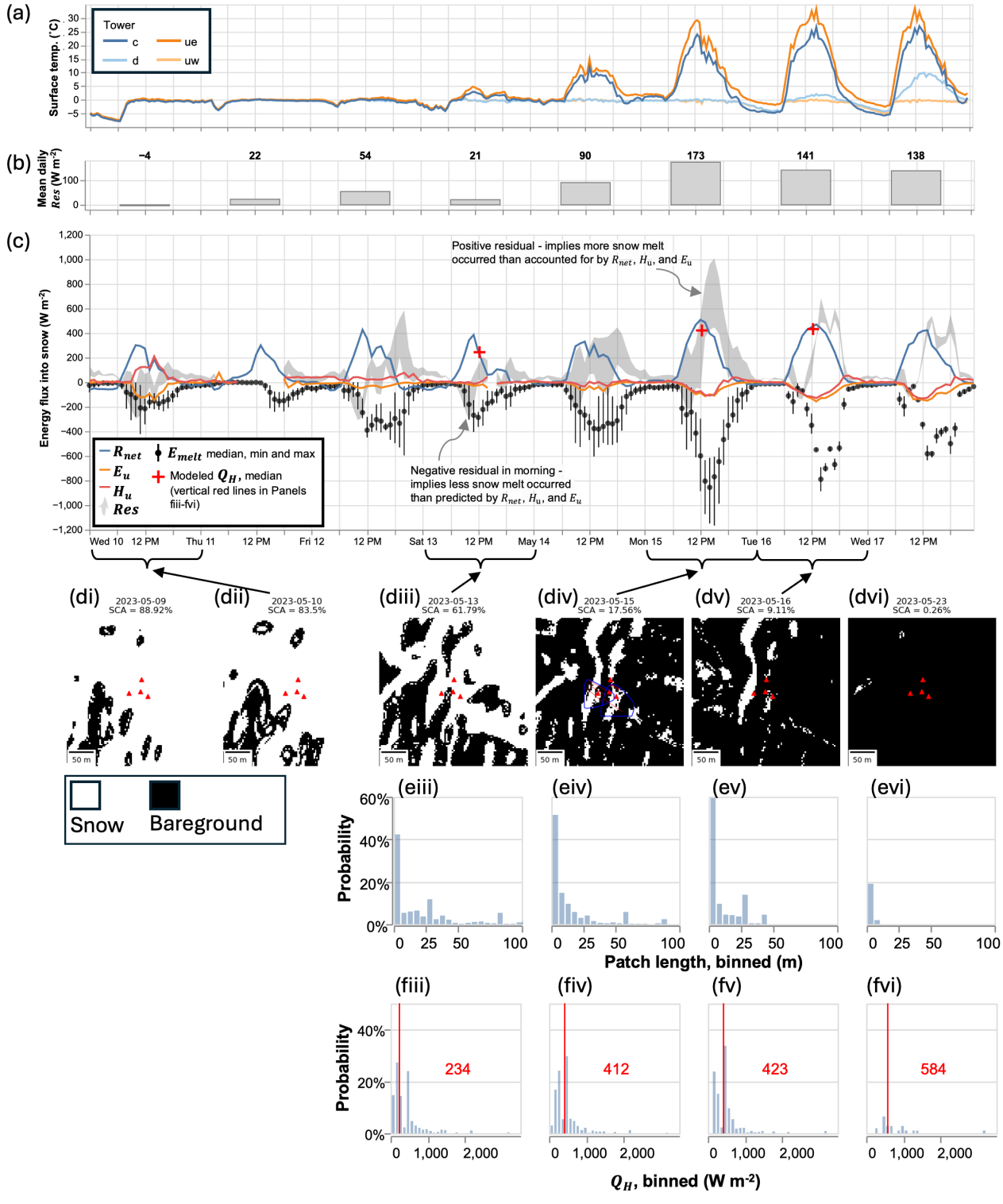

Figure 10. *Caption on next page.*

https://doi.org/10.5194/egusphere-2026-1633
Preprint. Discussion started: 18 May 2026

Figure 10. a) Time series of surface temperatures measured by four radiometers mounted on separate towers. b) The mean daily energy balance residual, Res, calculated from the hourly surface energy budget in panel c. c) Terms in the snow patch surface energy budget (Equation 7). We measured net radiation (R_{net}, blue line) (Section 3.3.2), vertical turbulent sensible heat flux over bare ground (H_u, red line), latent heat flux over bareground (E_u, orange line) (Section 3.3.3), and snow melt energy (E_{melt}, black dots and bars). We calculated E_{melt} by measuring the melt of six snow patch transects (see Figure 9); we show the median, minimum, and maximum measured melt rates. After 15 May, one patch melted out and the number of transects included in the melt estimates decreased from 6 to 3. We calculated Res (grey band) from the other energy fluxes (Equation 7. The spread in the grey band is calculated from the spread in E_{melt}. d) Snow covered area (SCA) maps from six days in May, overlapping with the study period. Includes copyrighted material of Planet Labs PBC. All rights reserved. e) Sample distribution of snow patch lengths calculated from the fSCA maps shown in the panels diii–dvi. No patch lengths are shown prior to 13 May because, prior to that date, snow cover was too large to estimate sensible heat advection. f) Distributions of Q_H for each day, created by calculating Q_H (Equation 5) for each patch length (panels eiii–evi). The vertical red line and red text denotes the median Q_H value.

According to our energy balance (Equations 6 and 7), positive Res indicates that horizontal sensible and latent heat advection (Q_H and Q_E, respectively) contributed to snow melt. To compare with the estimated Res, we estimated Q_H over the snow patches near our site. We only present results starting on 13 May, when fSCA dropped below 62%, because our advection model is not applicable for high fSCA (Section 3.1). We found that as fSCA decreased from 62% to 0.2% (Figure 10diii–dvi), snow patch length decreased (Figure 10eiii–evi) and Q_H increased from 234 to 584 W m^{-2} (Figure 10fiii–fvi). Modeled Q_H approximately matched the estimated Res on all days with both measurements (red crosses and grey band in Figure 10c).

We summarized the daily mean energy fluxes, daily maximum energy fluxes, and estimated mid-day Q_H in Table 1. On

		Daily mean			Daily max			Mid-day estimate
date	fSCA	E_{melt}	Res	R_{net}	E_{melt}	Res	R_{net}	Q_H
2023-05-14	–	-160	90	98	-453	267	331	–
2023-05-15	18%	-264	173	154	-851	668	508	412
2023-05-16	9%	-216	141	156	-790	588	470	423
2023-05-17	–	-187	138	132	-596	508	423	–

Table 1. Daily mean and maximum energy fluxes for the three largest energy flux terms in the energy balance, as shown in Figure 10c. We only include calculated values for days when fSCA was likely or confirmed less than 50%. Mid-day estimates of Q_H are the median value from Figures 10fiv – fv and should be compared with the Daily max values of the other terms.

15 and 16 May, two days with fSCA $< 50\%$, we estimated mid-day peak Res of 668 and 588 W m^{-2}, mid-day peak R_{net} of 508 and 473 W m^{-2}, and Q_H of 412 and 423, respectively. Q_H accounted for 62% and 72% of the mid-day peak energy balance residual and 81% and 89% of the mid-day peak net radiation. Overall, these estimates suggest that during patchy snow, horizontal sensible heat advection contributes to snow melt and can contribute a similar amount of energy as radiation.

https://doi.org/10.5194/egusphere-2026-1633
Preprint. Discussion started: 18 May 2026

4.5 Increased horizontal advection at the onset of patchy snow

When fSCA was high and snow mostly covered the landscape on 10 May, net radiation balanced snow melt, and Res was near zero (Figures 10b and c). At this time, advective effects were likely negligible at Kettle Ponds. This observation is consistent with previous studies that found snow melt is dominated by radiation early in the season (Mott et al., 2011). Between 14–17 May, when fSCA fell below 50%, Res became positive and modeled Q_H accounted for 62–72% of Res, suggesting that heat fluxes contribute more to snow melt as snow becomes increasingly patchy. Mott et al. (2011) also found that heat fluxes became increasingly important as the snow becomes patchy. While Mott et al. (2013) found that advection only contributed to snow melt when wind velocities exceed 5 m/s, local winds rarely exceeded this threshold during our study period (not shown), highlighting that advection processes are highly sensitive to local conditions and can vary across regions. Overall, our measurements strongly support the conclusion that Q_H contributes to the melting of patchy snow.

Previous studies found that horizontal latent heat advection, Q_E, can be on the same order of magnitude as Q_H (Harder et al., 2017; Van Der Valk et al., 2022). We did not estimate Q_E, although we found that Q_H only accounted for 62–72% of Res. It is possible that a portion of Res is due to Q_E, although, at our site, it appears that Q_E is smaller than Q_H. The contribution of Q_E to snow melt is also supported by the near-zero E_u values measured on 12–14 May (Figure 10c), which suggest that, within the footprint of the EC, evaporation over bare ground was balanced by condensation onto snow.

4.6 Limitations for estimating Q_H

To estimate Q_H over the distribution of snow patches near the measurement site, we used an equation fitted to measurements from just 30 minutes on 17 May. We then used this fitted equation to predict Q_H on four separate days, even though the fitted equation incorporates information about meteorological conditions, such as wind speed. For this reason, we were cautious to not over-interpret exact values of modeled Q_H. Future work should analyze the snow patch energy balance and incorporate Q_H modeled by more complex parameterizations (e.g. Harder et al., 2019)

4.7 Energy balance uncertainties

The close match between estimates of the energy balance residual and estimates of Q_H indicate that horizontal sensible heat advection contributes to snow melt at our site. However, our methods have some limitations, mainly uncertainty in estimates of the energy flux terms in Equation 7.

First, we believe we may be underestimating H_u and E_u. As discussed in Section 3.3.3, the two terms should represent heat fluxes over bare ground. However, we used ECs to estimate the two terms and an EC instrument over patchy snow integrates fluxes over both the snow-covered and bare ground surfaces within the EC footprint (as illustrated in Figure 3b). H_u is larger over bare ground than snow because the bare ground surface is warmer than the snow surface (Figure 10a). Additionally, E_u is likely larger over bare ground. The snow and bare ground surfaces were near saturation during our study period (Figure 4a, note the saturated muddy surface), and air adjacent to the bare ground surface has a higher humidity than over snow because it is warmer (warmer temperatures result in higher saturated vapor pressures). To estimate how much we may be underestimating

https://doi.org/10.5194/egusphere-2026-1633
Preprint. Discussion started: 18 May 2026

E_u and H_u, we used a bulk aerodynamic method to estimate H_u (Andreas et al., 2010) using measured bare ground surface temperatures (Figure 10a). We also attempted to use the bulk aerodynamic method to estimate E_u, but found the method produced erroneously large E_u estimates, and did not attempt to further constrain the uncertainty of E_u. The modeled H_u estimates were, at most, 50 W m^{-2} greater than measured H_u, which suggests we could be overestimating Res by 50 W m^{-2}.

Second, we considered potential uncertainties in our estimates of R_{net}, which likely stem from the two terms we estimated, LW_{out} and SW_{out}. To estimate LW_{out}, we assumed an emissivity of 0.98. Raleigh et al. (2013) suggested that snow emissivity rarely deviates from the range 0.97–1.0; thus, emissivity is only likely to affect our estimate of LW_{out} by 1–2 % (Equation 10). To estimate SW_{out}, we assumed a snow albedo of 0.6, which was the albedo over snow calculated by Lundquist et al. (2024) at our study site in early May. We recalculated our energy balance results using an albedo of 0.5, which reduced the daily mean Res on 15–17 by 20–26%. However, the decreased albedo led to unrealistically large negative residuals before 14 May, when we expected Res and advective fluxes to be near zero. Regardless, uncertainties in albedo could mean we are overestimating Res by around 25%.

Considering these sources of uncertainty, we find that we may be overestimating the Res term. However, this does not diminish the apparent importance of horizontal sensible heat advection, as our estimates of Res were generally larger than our estimates of Q_H (Table 1).

5 Conclusion

We measured horizontal sensible heat advection over patchy snow (Q_H) and its contribution to snow melt using a combination of high resolution measurements, including an infrared video camera, two scanning lidars, 3-meter resolution satellite imagery, and a suite of tower-based meteorological instruments.

Using an infrared video camera, we measured Q_H over a single snow patch and found that Q_H generally decreased with distance into the snow patch, consistent with theory. We also found that Q_H within 50 cm of the snow patch's upwind edge was less than Q_H predicted by theory, possibly due to flow effects created by the snow patch's shape or the rigid structure that held the measurement screen.

We estimated snow melt rates with both scanning lidars and snow pillows. We found that the lidar-based measurements matched snow pillow measurements and appeared to reliably measure the melt of scattered snow patches in topographic concavities. Snow pillows were less useful in our study, because they must be installed on flat ground, where snow generally melts out earlier. Our lidar-based measurements indicated that melt rates were higher at the upwind snow patch edge, and lower at the leeward edge, which is consistent with our infrared video camera measurements that showed Q_H decreasing with distance into the snow patch.

We used the lidar-based snow melt rates, estimates of net radiation, and eddy covariance measurements of vertical turbulent heat fluxes to characterize the surface energy balance of a snow patch. We also generated fractional snow covered area (fSCA) maps from 3-meter satellite imagery of our site, which allowed us to characterize the increasing patchiness of snow during our study period. As fSCA decreased and patchiness increased, the energy balance residual became increasingly large. When

https://doi.org/10.5194/egusphere-2026-1633
Preprint. Discussion started: 18 May 2026

fSCA was greater than 50%, the daily mean energy balance residual ranged from -4–54 W m^{-2}. When fSCA dropped below 50%, it ranged from 138–173 W m^{-2}.

Using all of our measurements, we characterized the surface energy balance and predicted Q_H on two days with fSCA < 50%. On these days, mid-day Q_H ranged from 412–423 W m^{-2}, peak mid-day net radiation ranged from 470–508 W m^{-2}, and the peak mid-day energy balance residual ranged from 588–668 W m^{-2}. These measurements suggest that horizontal advective fluxes of sensible heat contribute a similar amount of energy to snow melt as radiative fluxes on days with low fSCA. Q_H accounted for between 62–72% of the energy balance residual, which indicates that other processes also contributed to snow melt, such as horizontal latent heat advection.

Overall, our measurements strongly support the hypothesis that Q_H is an important component of the surface energy balance over patchy, melting snow. At our site, significant horizontal heat advection occurred for at least 4–5 days, when fSCA fell below 50% and the final snow patches melted away. These findings underscore the need to account for heat advection in models used to predict timing and rates of snow melt. Additionally, our measurements highlight the need for additional field measurements of heat advection, particularly in complex micro-topography such as depressions and concavities where snow patches persist. The IR video camera measurements of Q_H and lidar-based measurements of melting snow patches in topographic depressions revealed advection patterns and melt patterns that differ from previous studies. For further insight into heat advection on the snow-patch scale, the IR video camera method used here could be deployed over snow patches in variable topography, where advective fluxes are likely to deviate further from idealized models.

Data availability. Eddy covariance, surface meteorological measurements, and web-camera images from the Kettle Ponds site were collected as part of the Sublimation of Snow (SOS) campaign (Lundquist et al., 2024) and can be downloaded at the DOI link in this citation: NSF NCAR/EOL ISFS Team (2024). Infrared video camera data are available at this citation: Haugeneder et al. (2025). Lidar data are available upon request but are not publicly hosted due to their large volume. Fractional snow covered area maps are available as a supplement to the paper.

Appendix A: Derivation of the equation describing average sensible heat flux into a snow patch

We start with the conservation of heat in two dimensions (Equation 1), reorganized for convenience,

$$U\frac{\partial T}{\partial x} = \frac{1}{\rho c_p}\frac{\partial H}{\partial z} \qquad \Rightarrow \qquad U\rho c_p\frac{\partial T}{\partial x} = \frac{\partial H}{\partial z}. \tag{A1}$$

We now integrate from the surface ($z = 0$) to the top of the internal boundary layer or IBL ($z = z_b$),

$$\int_0^{z_b} U\rho c_p\frac{\partial T}{\partial x}\partial z = \int_0^{z_b}\frac{\partial H}{\partial z}\partial z, \tag{A2}$$

https://doi.org/10.5194/egusphere-2026-1633
Preprint. Discussion started: 18 May 2026

and find, with the fundamental theorem of calculus (FTC) applied on the right hand side (RHS),

$$\int_0^{z_b} U\rho c_p \frac{\partial T}{\partial x}\partial z = H(x,z_b) - H(x,0). \tag{A3}$$

Because the IBL height, $z_b(x)$, is defined as the height above the snow patch where the vertical sensible heat flux equals the vertical sensible heat flux over the upwind bareground, which we refer to as H_u, $H(x,z_b) = H_u$ and is constant,

$$\int_0^{z_b} U\rho c_p \frac{\partial T}{\partial x}\partial z = H_u - H(x,0). \tag{A4}$$

Now, we integrate over the horizontal domain, from the beginning of the snow patch ($x = 0$) to some distance into the snow patch ($x = X$),

$$\int_0^X \int_0^{z_b} U\rho c_p \frac{\partial T}{\partial x}\partial z\partial x = \int_0^X H_u \partial x - \int_0^X H(x,0)\partial x. \tag{A5}$$

Noting that H_u is constant, we find

$$\int_0^X H_u \partial x = X H_u. \tag{A6}$$

Now, we define the average value of $H(x,0)$ over the domain $x = [0, X]$ as $\langle H_0 \rangle$, and note that

$$\langle H_0 \rangle = \frac{1}{X}\int_0^X H(x,0)\partial x \qquad \Rightarrow \qquad X\langle H_0 \rangle = \int_0^X H(x,0)\partial x. \tag{A7}$$

Plugging Equations 6 and 7 into the RHS of Equation 5, we see that

$$\int_0^X \int_0^{z_b} U\rho c_p \frac{\partial T}{\partial x}\partial z\partial x = X H_u - X\langle H_0 \rangle. \tag{A8}$$

Now, we reorganize the left hand side (LHS) of the latest equation, noting that U is a function of z but not of x,

$$\rho c_p \int_0^{z_b} U \int_0^X \frac{\partial T}{\partial x}\partial x\partial z = X H_u - X\langle H_0 \rangle. \tag{A9}$$

Using the FTC, naming a new variable $T_u = T(0,z)$, and moving X to the LHS,

$$\frac{\rho c_p}{X}\int_0^{z_b} U(T(X,z) - T_u)\partial z = H_u - \langle H_0 \rangle. \tag{A10}$$

Note that the LHS of the equation is a horizontal flux of heat, which we call $-Q_H$,

$$-Q_H = H_u - \langle H_0 \rangle. \tag{A11}$$

https://doi.org/10.5194/egusphere-2026-1633
Preprint. Discussion started: 18 May 2026

and we reorganize to find

$$\langle H_0 \rangle = H_u + Q_H, \tag{A12}$$

which is Equation 2 in Section 3.1.

Appendix B: Estimating snow density during the melt season

We estimated snow density by combining measurements of SWE and snow depth over the tower C snow pillow. Snow density, ρ_{snow}, is calculated according to

$$\rho_{snow} = \frac{\text{SWE}}{\rho_w D}, \tag{B1}$$

where D is the snow depth. Measurements of SWE and snow depth demonstrate the melt out of snow above the tower C snow

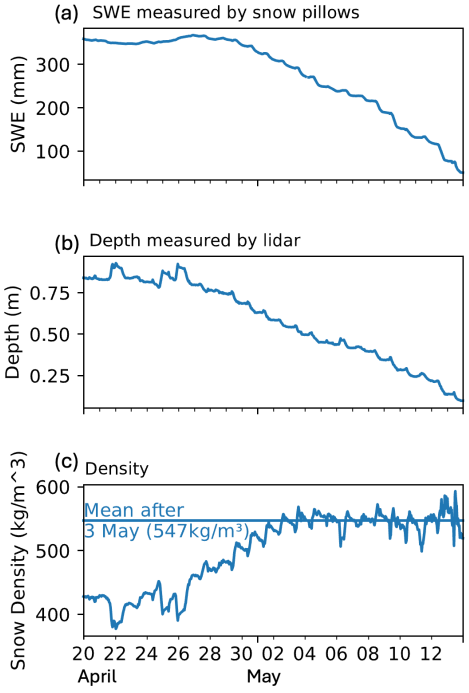

Figure B1. Measurements of snow properties between 20 April and 13 May 2023. a) Snow water equivalent (SWE) measured by the tower C snow pillow. b) Depth of snow on top of the tower C snow pillow, measured by scanning lidar. c) Snow density, calculated.

pillow (Figures B1a and B1b). Calculated density illustrates that snow density reached an upper threshold of approximately 550 kg/m^3 at the end of the melt season (Figure B1cx).

https://doi.org/10.5194/egusphere-2026-1633
Preprint. Discussion started: 18 May 2026

Author contributions. MH and DR collected and processed the infrared data, contributed to the analysis of the results, and reviewed and edited the manuscript. EG collected and processed the lidar data, and secured funding for the research. DLH contributed to the analysis of the results and reviewed and edited the manuscript. JDL supervised the work, reviewed and edited the manuscript, and secured funding for the research. ELS contributed to the analysis of the results and prepared the article with contributions from all co-authors.

Competing interests. The authors declare no competing interests.

Acknowledgements. We would like to thank Elie Bou-Zeid, Michelle DiBenedetto, Alex Horner-Devine, and Dale Durran for discussions that deepened our understanding and led to this publication. We also thank the Rocky Mountain Biological Laboratory for their facilitation of the field site. This work was supported by National Science Foundation Awards 2139836 and 2139809 and U.S. Department of Energy Environmental Systems Science award DE-SC0024075. Planet imagery was retrieved through NASA awards 80NSSC21K1151 and 80NSSC24K0050. This material is based upon work supported by the NSF National Center for Atmospheric Research, which is a major facility sponsored by the U.S. National Science Foundation under Cooperative Agreement No. 1852977. MH received funding from the Swiss National Science foundation under grant nr. 188554. We acknowledge the use of ChatGPT to improve writing style.

https://doi.org/10.5194/egusphere-2026-1633
Preprint. Discussion started: 18 May 2026

References

Andreas, E. L., Persson, P. O. G., Grachev, A. A., Jordan, R. E., Horst, T. W., Guest, P. S., and Fairall, C. W.: Parameterizing Turbulent Exchange over Sea Ice in Winter, Journal of Hydrometeorology, 11, 87–104, https://doi.org/10.1175/2009JHM1102.1, 2010.

Chiu, I., Pestana, S., Yang, K., Boudreau, E. T., Setiawan, L., Pflug, J., and Cristea, N.: PlanetSCA: A Python Package Implementing Snow-Covered Area Mapping PlanetScope Imagery with Machine Learning, https://doi.org/10.5281/ZENODO.17380192, 2025.

Claussen, M.: Local Advection Processes in the Surface Layer of the Marginal Ice Zone, Boundary-Layer Meteorology, 54, 1–27, https://doi.org/10.1007/BF00119409, 1991.

Cox, C. J., Intrieri, J. M., Butterworth, B. J., De Boer, G., Gallagher, M. R., Hamilton, J., Hulm, E., Meyers, T., Morris, S. M., Osborn, J., Persson, P. O. G., Schmatz, B., Shupe, M. D., and Wilczak, J. M.: Observations of Surface Energy Fluxes and Meteorology in the Seasonally Snow-Covered High-Elevation East River Watershed during SPLASH, 2021–2023, Earth System Science Data, 17, 1481–1499, https://doi.org/10.5194/essd-17-1481-2025, 2025.

Essery, R., Granger, R., and Pomeroy, J.: Boundary-layer Growth and Advection of Heat over Snow and Soil Patches: Modelling and Parameterization, Hydrological Processes, 20, 953–967, https://doi.org/10.1002/hyp.6122, 2006.

Foken, T., Wimmer, F., Mauder, M., Thomas, C., and Liebethal, C.: Some Aspects of the Energy Balance Closure Problem, Atmospheric Chemistry and Physics, 6, 4395–4402, https://doi.org/10.5194/acp-6-4395-2006, 2006.

Fujita, K., Hiyama, K., Iida, H., and Ageta, Y.: Self-regulated Fluctuations in the Ablation of a Snow Patch over Four Decades, Water Resources Research, 46, 2009WR008 383, https://doi.org/10.1029/2009WR008383, 2010.

Granger, R. J., Pomeroy, J. W., and Parviainen, J.: Boundary-layer Integration Approach to Advection of Sensible Heat to a Patchy Snow Cover, Hydrological Processes, 16, 3559–3569, https://doi.org/10.1002/hyp.1227, 2002.

Granger, R. J., Essery, R., and Pomeroy, J. W.: Boundary-layer Growth over Snow and Soil Patches: Field Observations, Hydrological Processes, 20, 943–951, https://doi.org/10.1002/hyp.6123, 2006.

Grudzielanek, A. M. and Cermak, J.: Capturing Cold-Air Flow Using Thermal Imaging, Boundary-Layer Meteorology, 157, 321–332, https://doi.org/10.1007/s10546-015-0042-8, 2015.

Harder, P., Pomeroy, J. W., and Helgason, W.: Local-Scale Advection of Sensible and Latent Heat During Snowmelt, Geophysical Research Letters, 44, https://doi.org/10.1002/2017GL074394., 2017.

Harder, P., Pomeroy, J. W., and Helgason, W. D.: A Simple Model for Local-Scale Sensible and Latent Heat Advection Contributions to Snowmelt, Hydrology and Earth System Sciences, 23, 1–17, https://doi.org/10.5194/hess-23-1-2019, 2019.

Haugeneder, M., Lehning, M., Reynolds, D., Jonas, T., and Mott, R.: A Novel Method to Quantify Near-Surface Boundary-Layer Dynamics at Ultra-High Spatio-Temporal Resolution, Boundary-Layer Meteorology, 186, 177–197, https://doi.org/10.1007/s10546-022-00752-3, 2023.

Haugeneder, M., Hogan, D., Schwat, E., Lundquist, J., Gutmann, E., and Vano, J.: SOS: Thermal IR Data. Version 1.0, https://doi.org/10.26023/EA6S-AP37-YV10, 2025.

Kochendorfer, J. and Paw U, K. T.: Field Estimates of Scalar Advection across a Canopy Edge, Agricultural and Forest Meteorology, 151, 585–594, https://doi.org/10.1016/j.agrformet.2011.01.003, 2011.

Liston, G. E.: Local Advection of Momentum, Heat, and Moisture during the Melt of Patchy Snow Covers, Journal of Applied Meteorology, 34, 1705–1715, https://doi.org/10.1175/1520-0450-34.7.1705, 1995.

https://doi.org/10.5194/egusphere-2026-1633
Preprint. Discussion started: 18 May 2026

Lundquist, J. D., Vano, J., Gutmann, E., Hogan, D., Schwat, E., Haugeneder, M., Mateo, E., Oncley, S., Roden, C., Osenga, E., and Carver, L.: Sublimation of Snow, Bulletin of the American Meteorological Society, https://doi.org/10.1175/BAMS-D-23-0191.1, 2024.

Mahrt, L. and Vickers, D.: Boundary-Layer Adjustment Over Small-Scale Changes of Surface Heat Flux, Boundary-Layer Meteorology, 116, 313–330, https://doi.org/10.1007/s10546-004-1669-z, 2005.

Mahrt, L., Nilsson, E., Rutgersson, A., and Pettersson, H.: Vertical Divergence of the Atmospheric Momentum Flux near the Sea Surface at a Coastal Site, Journal of Physical Oceanography, 51, 3529–3537, https://doi.org/10.1175/JPO-D-21-0081.1, 2021.

Mott, R., Egli, L., Grünewald, T., Dawes, N., Manes, C., Bavay, M., and Lehning, M.: Micrometeorological Processes Driving Snow Ablation in an Alpine Catchment, The Cryosphere, 5, 1083–1098, https://doi.org/10.5194/tc-5-1083-2011, 2011.

Mott, R., Gromke, C., Grünewald, T., and Lehning, M.: Relative Importance of Advective Heat Transport and Boundary Layer Decoupling in the Melt Dynamics of a Patchy Snow Cover, Advances in Water Resources, 55, 88–97, https://doi.org/10.1016/j.advwatres.2012.03.001, 2013.

Mott, R., Daniels, M., and Lehning, M.: Atmospheric Flow Development and Associated Changes in Turbulent Sensible Heat Flux over a Patchy Mountain Snow Cover, Journal of Hydrometeorology, 16, 1315–1340, https://doi.org/10.1175/JHM-D-14-0036.1, 2015.

Mott, R., Paterna, E., Horender, S., Crivelli, P., and Lehning, M.: Wind Tunnel Experiments: Cold-Air Pooling and Atmospheric Decoupling above a Melting Snow Patch, The Cryosphere, 10, 445–458, https://doi.org/10.5194/tc-10-445-2016, 2016.

Mott, R., Schlögl, S., Dirks, L., and Lehning, M.: Impact of Extreme Land Surface Heterogeneity on Micrometeorology over Spring Snow Cover, Journal of Hydrometeorology, 18, 2705–2722, https://doi.org/10.1175/JHM-D-17-0074.1, 2017.

Mott, R., Vionnet, V., and Grünewald, T.: The Seasonal Snow Cover Dynamics: Review on Wind-Driven Coupling Processes, Frontiers in Earth Science, 6, 197, https://doi.org/10.3389/feart.2018.00197, 2018.

NSF NCAR/EOL ISFS Team: SOS: ISFS Surface Meteorology and Flux Products. Version 1.1, https://doi.org/10.26023/CYK2-SR3N-880J, 2024.

PBC, P. L.: Planet Application Program Interface: In Space for Life on Earth, 2020/2025.

Pestana, S., Chickadel, C. C., Harpold, A., Kostadinov, T. S., Pai, H., Tyler, S., Webster, C., and Lundquist, J. D.: Bias Correction of Airborne Thermal Infrared Observations Over Forests Using Melting Snow, Water Resources Research, 55, 11 331–11 343, https://doi.org/10.1029/2019WR025699, 2019.

Pflug, J. M. and Lundquist, J. D.: Inferring Distributed Snow Depth by Leveraging Snow Pattern Repeatability: Investigation Using 47 Lidar Observations in the Tuolumne Watershed, Sierra Nevada, California, Water Resources Research, 56, e2020WR027 243, https://doi.org/10.1029/2020WR027243, 2020.

Raleigh, M. S., Landry, C. C., Hayashi, M., Quinton, W. L., and Lundquist, J. D.: Approximating Snow Surface Temperature from Standard Temperature and Humidity Data: New Possibilities for Snow Model and Remote Sensing Evaluation, Water Resources Research, 49, 8053–8069, https://doi.org/10.1002/2013WR013958, 2013.

Schirmer, M., Wirz, V., Clifton, A., and Lehning, M.: Persistence in Intra-annual Snow Depth Distribution: 1. Measurements and Topographic Control, Water Resources Research, 47, 2010WR009 426, https://doi.org/10.1029/2010WR009426, 2011.

Schwat, E., Hogan, D., Paw U, K. T., Cox, C. J., Butterworth, B. J., Gutmann, E., Vano, J. A., and Lundquist, J. D.: Estimating Snow Sublimation in Complex Terrain: A Season of Intensive Field Measurements and the Role of Vertical Water Vapor Flux Divergence, Journal of Hydrometeorology, https://doi.org/10.1175/JHM-D-25-0022.1, 2025.

https://doi.org/10.5194/egusphere-2026-1633
Preprint. Discussion started: 18 May 2026

Sorteberg, H., Engeset, R., and Udnæs, H.: A National Network for Snow Monitoring in Norway: Snow Pillow Verification Using Observations and Models, Physics and Chemistry of the Earth, Part C: Solar, Terrestrial & Planetary Science, 26, 723–729, https://doi.org/10.1016/S1464-1917(01)95016-0, 2001.

Stiperski, I. and Rotach, M. W.: On the Measurement of Turbulence Over Complex Mountainous Terrain, Boundary-Layer Meteorology, 159, 97–121, https://doi.org/10.1007/s10546-015-0103-z, 2016.

Thomas, C. K.: Variability of Sub-Canopy Flow, Temperature, and Horizontal Advection in Moderately Complex Terrain, Boundary-Layer Meteorology, 139, 61–81, https://doi.org/10.1007/s10546-010-9578-9, 2011.

Van Der Valk, L. D., Teuling, A. J., Girod, L., Pirk, N., Stoffer, R., and Van Heerwaarden, C. C.: Understanding Wind-Driven Melt of Patchy Snow Cover, The Cryosphere, 16, 4319–4341, https://doi.org/10.5194/tc-16-4319-2022, 2022.

Weisman, R. N.: Snowmelt: A Two-dimensional Turbulent Diffusion Model, Water Resources Research, 13, 337–342, https://doi.org/10.1029/WR013i002p00337, 1977.

Wieringa, J.: Representativeness of Wind Observations at Airports, Bulletin of the American Meteorological Society, 61, 962–971, https://doi.org/10.1175/1520-0477(1980)061<0962:ROWOAA>2.0.CO;2, 1980.

Yang, K., John, A., Shean, D., Lundquist, J. D., Sun, Z., Yao, F., Todoran, S., and Cristea, N.: High-Resolution Mapping of Snow Cover in Montane Meadows and Forests Using Planet Imagery and Machine Learning, Frontiers in Water, 5, 1128 758, https://doi.org/10.3389/frwa.2023.1128758, 2023.